High-resolution monitoring of the initial development of cracks in experimental masonry shear walls and their reproduction in finite element models

Korswagen Eguren, Paul; Longo, Michele; Rots, Jan G.

DOI
10.1016/j.engstruct.2020.110365

Publication date
2020

Document Version
Final published version

Published in
Engineering Structures

Engineering Structures 211 (2020) 110365

Contents lists available at ScienceDirect

Engineering Structures

journal homepage: www.elsevier.com/locate/engstruct

High-resolution monitoring of the initial development of cracks in experimental masonry shear walls and their reproduction in finite element models

Paul A. Korswagen*, Michele Longo, Jan G. Rots

Delft University of Technology, Faculty of Civil Engineering, Stevinweg 1, Delft, 2826 CN, the Netherlands

ARTICLE INFO

Keywords:
Shear wall
Clay masonry
Light damage
Cracks
DIC
FEM

ABSTRACT

Induced seismicity in the north of the Netherlands has recently exposed unprepared, unreinforced masonry structures to considerable earthquake hazard. While the ultimate-limit state capacity of the structures is vital to assess the individual's risk, their behaviour during more frequent, lighter earthquakes leading to 'light damage', has shown to be strongly linked to economical losses and societal unrest. To study the effect of these repeated light earthquakes, the behaviour of masonry structures, typical of the region, needs to be investigated when subjected to multiple small cycles. In particular, insight into the potential aggravation of the light damage is sought. Hence, shear walls of replicated clay brick masonry have been tested in the laboratory and exposed to a high number of low in-plane drift cycles. The experiments show, under inspection with high-resolution Digital Image Correlation, how stair-case, diagonal cracks initially distribute in multiple cracks running in joints at the centre of the walls, but later localise into a single, visible, wider crack. The tests are used to establish an interval over which light damage can be expected for these types of walls.

Furthermore, this initial distribution of strains in 'bands' and subsequent localisation, previously observed only with computational finite element models and which could not be verified experimentally, is compared and reproduced with improved models both at the composite continuum scale (macro-model) and the brick-to-brick micro scale. The models are calibrated based on the quasi-static, cyclic experimental results and later used for extrapolation in dynamic nonlinear settings to assess the influence of natural ground motion excitations.

1. Introduction

Human-induced earthquakes have become a hazard in the north of the Netherlands over the past decades. The extraction of natural gas from reservoirs underneath the ground has produced seismic events that have led to peak ground accelerations of approximately 0.1 g in some occasions, with many more events at lower vibration values [32,2,31]. These light but frequent earthquakes have raised concerns about the behaviour of structures in the region, lately especially in regard to the light damage or serviceability state of the structures, in many cases leading to economical losses and societal unrest [43,47,40]. In particular, the unreinforced masonry structures, ubiquitous in the province of Groningen, in the north of the Netherlands, seem to be vulnerable to displaying seismic damage [9,10]. In consequence, prior research has focused in characterising the ultimate limit state of the structures and determining their behaviour during anticipated, heavy seismic events; this has been done extensively as shown by, for instance: van Elk et al. [46], who detail the multiple steps between assessing seismicity and building fragility; Messali et al. [29], who present a multi-scale approach towards characterising the ultimate limit state of Dutch masonry structures; Esposito et al. [13], who performed quasi-static pushover tests on a full-scale clay masonry structure; or Graziotti et al. [18], who conducted dynamic tests of a similar structure. Moreover, literature comparable to the Dutch case is also extensive: a comprehensive review of such studies is performed by Morandi et al. [30], who gather an ample overview of masonry in-plane tests, some with material, loading, and boundaries similar to the walls tested herein.

Yet, to understand the initiation and propagation of light damage during the more commonly occurring (or occurred) seismic events, additional research is needed. This is because the existing literature observing the near-collapse state, while mentioning light damage as a side note, does not consider for instance, the propagation and accumulation of damage during repeated low vibrations nor does it measure

* Corresponding author.
E-mail address: p.a.korswageneguren@tudelft.nl (P.A. Korswagen).

https://doi.org/10.1016/j.engstruct.2020.110365
Received 5 August 2019; Received in revised form 14 January 2020; Accepted 10 February 2020

the aesthetic importance of the damage (e.g. [14,20,45]).

Other literature which does characterise damage with cracks and looks at its categorisation considers material that differs from the one representative of Groningen masonry, or does not observe crack propagation in fine detail (e.g. [12,16,34]). A study similar to the one presented herein, detailed in Korswagen et al. [21,22], has looked into light damage with cracks propagating from the corner of windows and in walls that act mainly in flexure. However, the behaviour of walls without openings, which are common as division walls between and at the side of terraced houses (a.k.a. row-houses or townhouses) or as a part of detached houses, commonly denoted squat or shear walls, where cracks initiate at the centre of the walls and propagate outwards, has not yet been investigated with the propagation of small cracks as a focus. This is thus the priority of this article: to look into the cumulative propagation of narrow cracks in unreinforced clay masonry walls acting mainly in shear.

Testing and finite element modelling of double-clamped masonry shear walls with a view to damage is not new. Anthoine et al. [1] for example, performed cyclic laboratory experiments on such walls and successfully determined, both experimentally and numerically, that damage focuses at the edges and at the centre of the walls. Magenes and Calvi [27] conducted similar tests. Yet both studies were focused on the ultimate capacity of the walls and did not contemplate any cumulative light damage. Then, Bosiljkov et al. [6] for instance, did look at the possible crack patterns in similar types of walls and set drift values for damage limitation (in some aspects comparable to light damage or damage state 1, DS1), but again, no cumulation was considered and the main focus was on the ultimate behaviour of the walls. Petry and Beyer [34] and Graziotti et al. [17] also tested squat walls and observed typical shear patterns, and Schreppers et al. [41] further referred to the computational implementation of these and similar tests. Still, the initiation of the cracks, from a wide band to the localisation into a single crack as observed in some early numerical studies [37], a phenomenon occurring at the start of the propagation of damage, has been seen experimentally in some recent studies on full-scale walls [34], but has not been reported to occur as a result of cumulative damage effects. This article considers the experimental testing of double-clamped masonry walls monitored with high-resolution digital image correlation (DIC) to detect the formation and cumulative propagation of cracks already at drift values below 0.05%, and their significance for the strength of the walls. DIC is a photogrammetry technique (see for example [4,8,24]), has been successfully used by many studies to observe the behaviour of masonry at various scales (eg. [44,11,12]), and is expanded herein to “high-resolution” for imperceptible cracks over a large area.

The article starts with a description of the tests in chapter 2, followed by their results and discussion in chapter 3. Later, chapter 4 delves into the finite element modelling of these walls, both with a constitutive macro-material model with a smeared cracking approach, and with a micro-model allowing for discrete cracks at the brick-mortar interfaces. Then, chapter 5 assesses damage on the walls using the calibrated model and a time-history analysis with seismic ground motion.

2. setup of laboratory tests

Two nominally-identical, full-scale walls (see Figs. 1 and 2) were tested in-plane under a pre-compression stress of 0.46 MPa and a displacement-controlled, cyclically-increasing lateral drift. The walls, denoted TUD-Comp47 and Comp48, were single-wythe (100 mm) and approximately 3.1 m in width and 2.7 m in height. Each wall was fixed to a bottom steel beam and to a top steel beam. The overburden value was chosen to mimic the load of ground-floor party walls of typical Dutch terrace houses, but slightly adjusted to guarantee stability of the experimental setup when maintaining the double-clamped condition. Two pairs of vertically oriented hydraulic jacks were configured such that the overburden was kept constant at the predefined value while the bottom and top beam were kept parallel (double-clamped boundary), thus only allowing for an in-plane, lateral translation of the top of the walls. Additional details about the experimental setup of the walls can be found in Messali and Rots [28]. The specimens were built to replicate baked clay-brick masonry as found in the Groningen area. A characterisation campaign was conducted to establish the material properties of the existing masonry and build laboratory equivalents of these, see Jafari et al. [19].

The DIC pattern on the wall, consisting of random speckles or dots, allowed for the monitoring of the full displacement field of the wall in a grid with a spacing of 2.6 × 2.6 mm and a precision of 20 μm, comprising over 1.2 million measurement (or grid) points. Images were taken at precise time-points throughout the test with a 51 Mpx DSLR camera and a 35 mm lens stopped down to f/9.0. Shots were illuminated with a flash at a speed of 1/63,000 s to produce even lighting conditions and eliminate image blur. The setup, in combination with the optimised speckle pattern and the DIC-algorithm developed for these kind of tests, allowed for the observation and, most importantly, the progression (in width and in length) of cracks invisible to the naked eye over the entire surface of the full-scale wall. This has herein been considered as high-resolution.

DIC was thus used to detect the propagation of cracks observing any increase in crack width. Since this implementation of DIC outputs the horizontal and vertical displacement of any measurement point, subtracting the displacement of neighbouring points in the horizontal and vertical directions results in the vertical and horizontal, closing or opening displacement between both points which is usually associated to cracks in the bed and head joints. The opening between two points can be considered a crack when it exceeds a given threshold, and is herein considered a visible crack when it exceeds 0.1 mm in width. This was done automatically for the millions of points surveyed, and neighbouring ‘cracked’ points were gathered into the notion of cracks.

Then, the crack pattern at a given instance during the test was characterised with a damage parameter that determines the damage intensity based on the number, width, and length of the cracks following Eq. (1). The damage parameter Psi (Ψ) is based on a scale that defines the ease of repair of the cracks adapted from [5], Burland et al. (1974), and, at its latest, [15]. Here, the total of visible cracks is expressed in one number such that the narrowest visible cracks with a width of 0.1 mm result in a value of around one (Ψ = 1), slightly larger cracks of close to 1 mm width correspond to two (Ψ = 2) and cracks of approximately 4 mm in width give a value of three (Ψ = 3). This range of visible cracks from Ψ = 1 to Ψ = 3 is herein described as light damage (DS1). Additional information regarding this damage parameter can be found in Korswagen et al. [21,22]. In this manner, Psi (Ψ) can be computed from both DIC and FEM data analogously: in the former by differentiating the displacement fields to obtain the crack width, and in the latter by employing the crack width data directly produced by finite element models with cracking material models (see later Section 4.1).

$$\Psi = 2 \cdot n_c^{0.15} \cdot \hat{c}_w^{0.3} \quad \text{with} \quad \hat{c}_w = \frac{\sum_{i=1}^{n_c} c_{w,i}^2 \cdot c_{L,i}}{\sum_{i=1}^{n_c} c_{w,i} \cdot c_{L,i}} \tag{1}$$

where n_c is the number of cracks in the wall/specimen $\hat{c}_w$ is the width-weighted and length-averaged crack width (in mm) calculated with: c_w, the maximum crack width along each crack in mm and c_L, the crack length in mm. For $n_c = 1$, $\hat{c} = c_w$. In this expression, the crack width of each crack is measured at their widest point.

The walls were tested with a cyclically increasing lateral in-plane drift. However, the cycles were asymmetric, as the amplitude in the positive drift direction was twice as large as in the negative direction (see signs in Fig. 1). The asymmetry of the loading protocol was inspired by real earthquake ground motion as monitored for the Zeerijp 2018 earthquake and was purposely chosen to foster a detectable accumulation of damage. Moreover, a large number of identical cycles

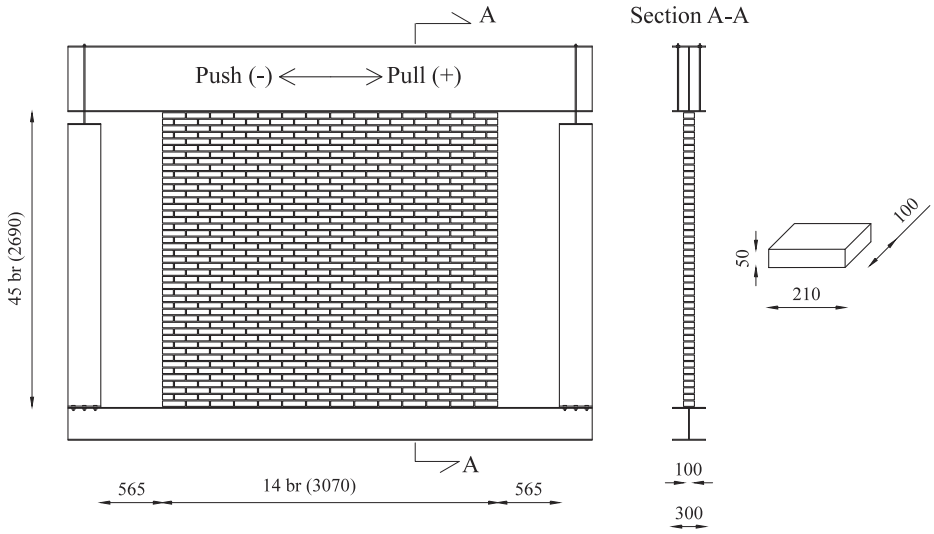

Fig. 1. Geometry of the shear walls.

was selected for each stepwise drift to be able to assess the propagation of damage under repeated loading. This is explained in Fig. 3.

First, the time series of the maximum rotated component of the horizontal acceleration as recorded at the station of Garsthuizen (BGAR) for the Zeerijp earthquake of the 8 of January of 2018 is plotted together with the parameter of Arias intensity (Fig. 3a). As can be observed, most of the energy is released in a short time (Fig. 3b). The ground displacement associated with this time span is shown then in Fig. 3c. Finally, considering that the inter-storey displacement seldom matches the ground displacement, Fig. 3d shows the approximated, chosen quasi-static drift profile. This asymmetric profile constitutes one cycle in the loading protocol and is then repeated 10 times per step, for a total of 6 incremental steps starting at 0.27‰ of maximum in-plane lateral drift, and increasing 0.065‰ every step until 0.69‰ (Fig. 3e).

The initial value of drift (0.27‰ or $2.7{\cdot}10^{-4}$ which corresponds to 0.27 mm/m) was determined experimentally to correspond to the initiation of light damage defined to be in the range of $1 < \Psi < 3$ for DS1. The first wall was displaced monotonically in increments of 0.025‰ and the crack initiation was evaluated live with DIC on the entire surface of the walls and at certain locations with linear potentiometers placed on the back of the wall. A rocking crack was detected at the top of the wall and the drift corresponding to a width of 0.1 mm (over a length of 100 mm) of this crack was applied as the initial value of drift for both walls (0.27‰), i.e. in step 1, and subsequently incremented up to 0.69‰ in step 6.

3. Results and discussion of laboratory tests

The force measured throughout the two tests was recorded and is plotted against the applied value of lateral, in-plane drift in Fig. 4 (parts a and c respectively). Additionally, the maximum force for each peak in the protocol is extracted and shown in Fig. 4b and d. Fig. 4a also shows an additional seventh step performed for specimen Comp47. First, Fig. 4a and c show that both walls behaved quite similarly, with incursions into the non-linear regime in the positive drift direction but remaining fairly linear in the negative direction; the hysteresis of the graphs is small, consistent with light damage, as is the limited softening post-peak. Yet, Fig. 4b and d show that there is also a consistent degradation in strength for every cycle, starting at the second step, but only in the positive direction. Even for the negative peaks reaching base shear forces higher than their positive peak counterparts, the degradation is minimal in contrast to the lower positive peaks that do display a slight degradation in strength. The degradation is in the order of 10% and reaches a maximum during the seventh extra step performed in the test of Comp47. Moreover, the reduction in strength was initially greater and stabilised towards the end of each step.

The deformation of the specimens as shown in Fig. 5 reveals a typical shear behaviour, mixed with crack openings in the core of the walls. Note that the walls seem to rotate but the top and bottom remain mostly parallel (as a result of the enforcing of the double-clamped condition). The drift is computed as the actual drift occurring on the

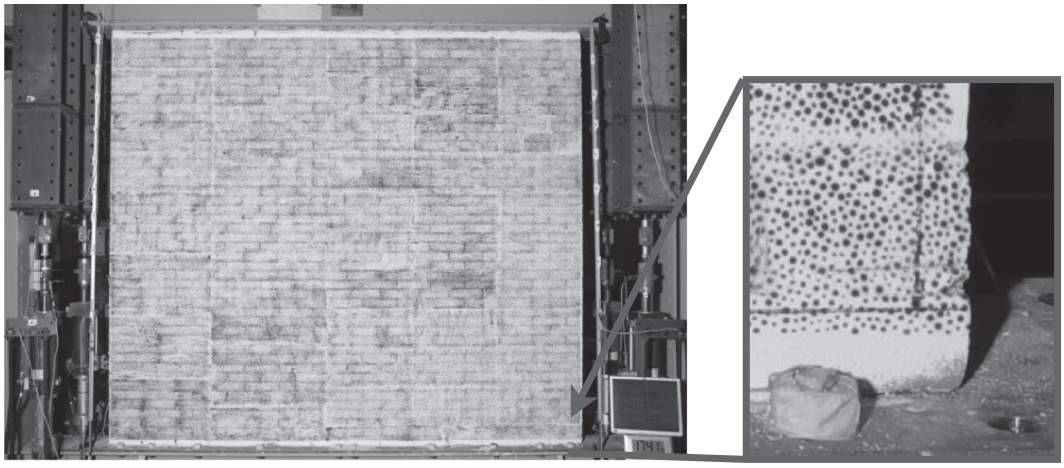

Fig. 2. Photo of one of the two walls painted with a pattern apt for DIC and zoomed-in crop of the pattern.

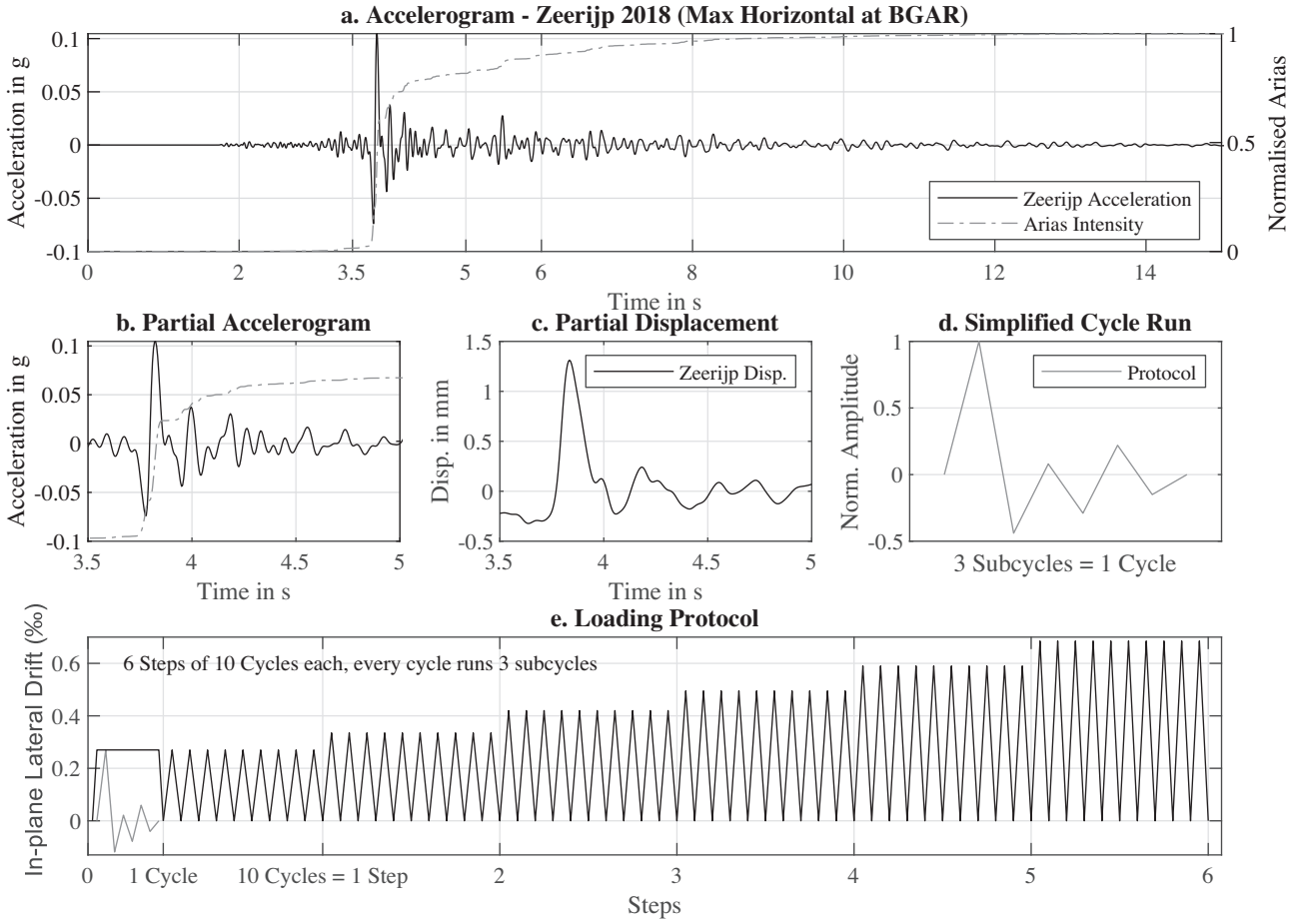

Fig. 3. Derivation and loading protocol for the shear walls: (a) accelerogram for typical Groningen earthquake, maximum rotated horizontal component of Zeerijp (January of 2018) earthquake registered at the BGAR station, (b) Zoom-in of (a), (c) displacements corresponding to (b), (d) simplified cycle run representing (c), and (e) total loading protocol, as series of subcycles, cycles and steps.

wall thus compensating for this rigid body rotation in a way similar to Lagomarsino [23]. The deformation also reveals the asymmetry of the protocol with mostly linear shear deformation in the negative direction and non-linear (crack opening) in the positive direction. The crack propagation at the maximum positive drift is detailed in Fig. 6 where the strains in the displacement field captured with DIC are contrasted for the end of each step. Ignoring the random noise displayed in these highly sensitive graphs, one can observe how cracks focus at the mortar interface. Moreover, it is fairly clear that cracks initially appear smeared over a few parallel joints and later localise into a single, “darker” line of joints or into an array of overlapping darker lines. Furthermore, it is only in step 7 where the crack finally cuts through a brick in order to complete the ultimate shear failure mechanism as seen in other studies.

The opening of the cracks is interpreted and displayed in Fig. 7 for the entire tests. Here, continuous cracks are considered as a single crack, though the criterion employed is disputable: the entire crack in the body of the wall could also be considered to be one crack. Nevertheless, it is shown subdivided to better illustrate the width and propagation of the different sections of the crack. The graphs in Fig. 7 show that cracks propagate not only at the change of step when the maximum drift is increased, but also within a step when the drift remains the same. This is particularly the case towards the end of the two tests when the cracks grow in width and especially in length.

Both walls first exhibited a rocking crack at the top (crack 1) which remained the widest throughout both tests reaching a crack width value of 0.8 mm for Comp47 and 0.55 mm for Comp48, see Fig. 7. The second wall developed a second body crack (crack 2) which constrained the width and length of the rocking crack. Barring this dissimilitude, both walls exhibited a main shear cracking zone at an angle of 55° to the horizontal with a maximum width of 0.5 mm. Since the masonry joints allow for diagonal cracks at an angle of only 29°, the main body crack was formed by multiple shorter cracks which, during the light damage stage, did not interconnect through the bricks but remained parallel to each other albeit shifted to allow for the overall 55° inclination of the crack. The body crack was widest at its core (see crack 5 and crack 7 for the first and second wall, respectively) and narrowest at the extremes towards the top and bottom edges of the wall (see crack 6 of both walls, for example). The body crack became visible (with a width larger than 0.1 mm), at a drift of approximately 0.5‰ for the first wall and 0.4‰ for the second.

Since the wall was glued with epoxy to the steel beams, the potential rocking cracks had to occur at the first mortar interface as is shown in Fig. 6, yet no rocking crack was detected at the bottom. Fig. 6 shows a small crack, perhaps one brick in length, during the test of Comp47, but it did not extend further (see also Fig. 5). Presumably, the lack of a rocking crack at the bottom is due to the imperfect boundary conditions of the test setup, but this is not known for certain. The crack in the body of the wall, however, was well defined and followed a similar path in both walls. A force flow analysis, see Fig. 8, reveals that the path is consistent with the inclination of the force resultant on the wall comprised by the vertical and lateral loads. This poses the crack as a combination of shear and splitting. The crack is propagated incrementally over the multiple cycles and steps, and, because the negative drift achieves only half of the amplitude of the positive drift, the crack appears to never fully close, thus growing by incrementally

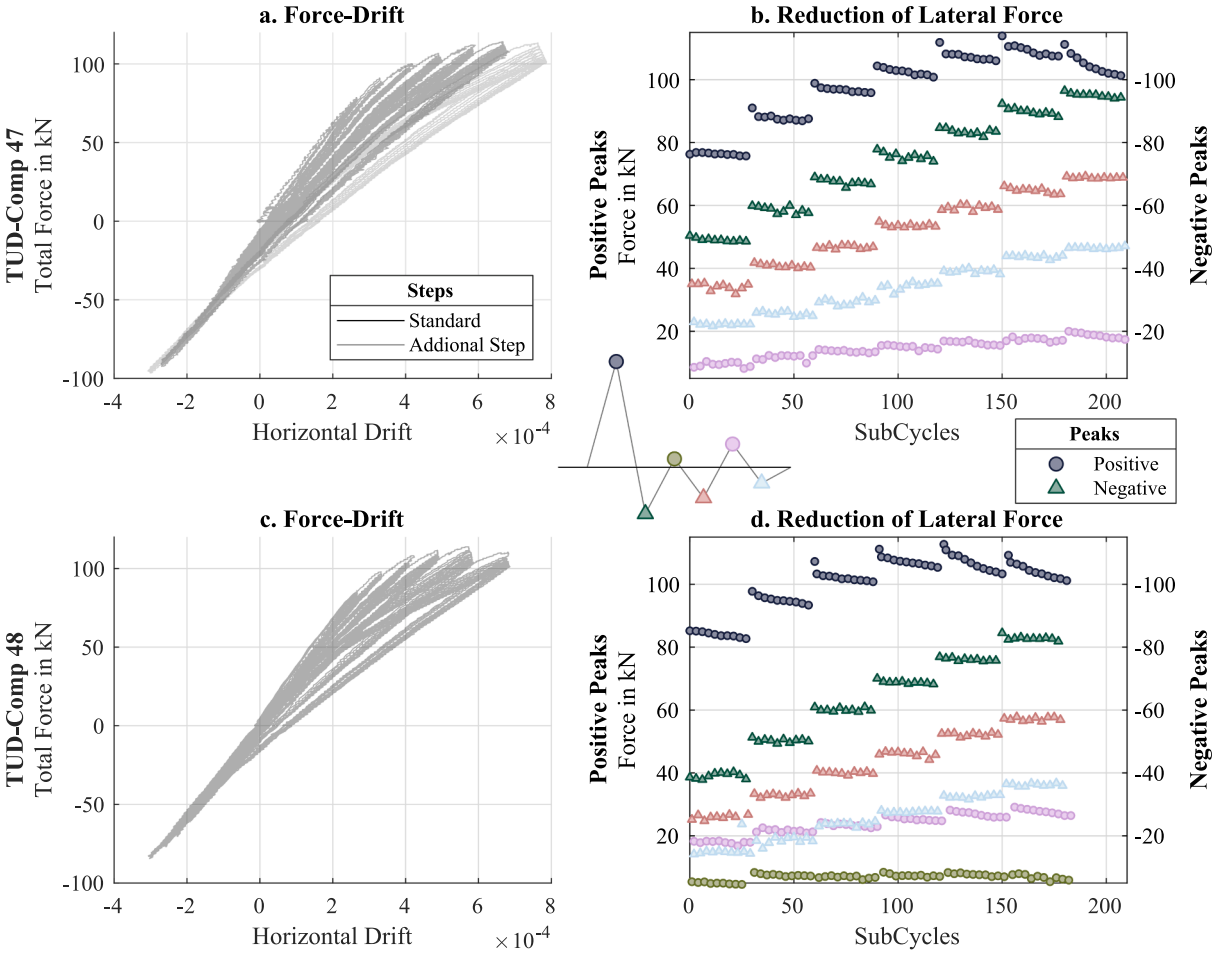

Fig. 4. Force-drift curves (a, c) and reduction of the maximum force attained during each cycle (b, d). (a, b) for the Comp47 test and (c, d) for the Comp48 test. Centre scheme shows subcycle notation of each subcycle, see also Fig. 3.

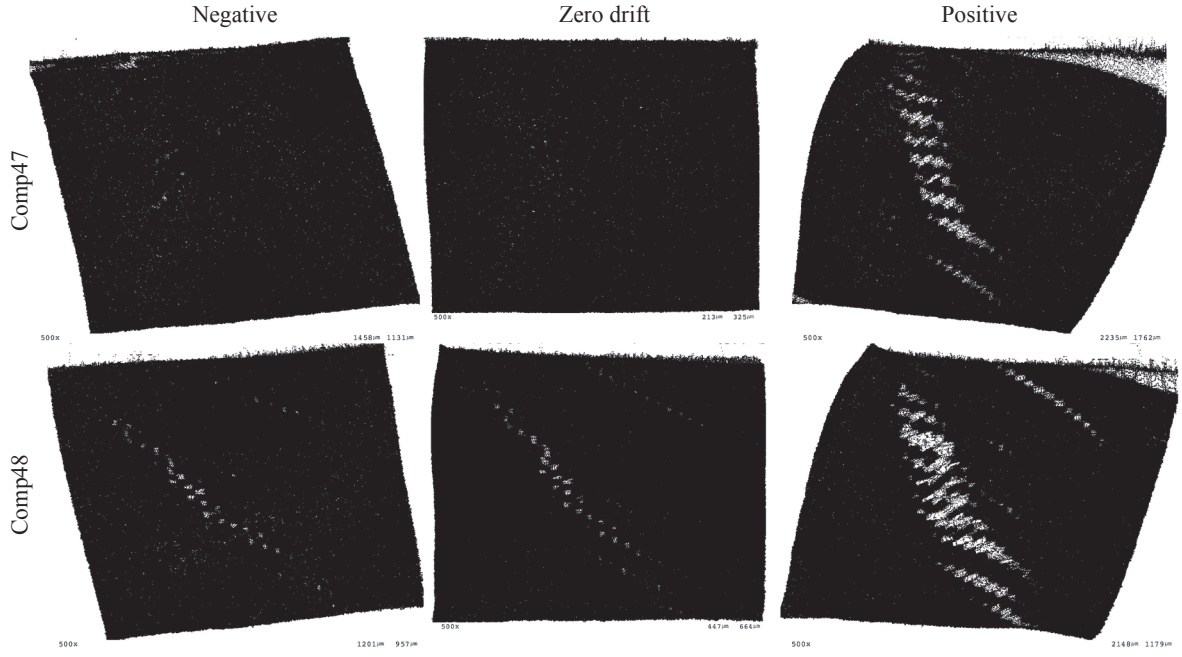

Fig. 5. Deformed shape magnified 500 times for the end of the sixth step as captured with DIC.

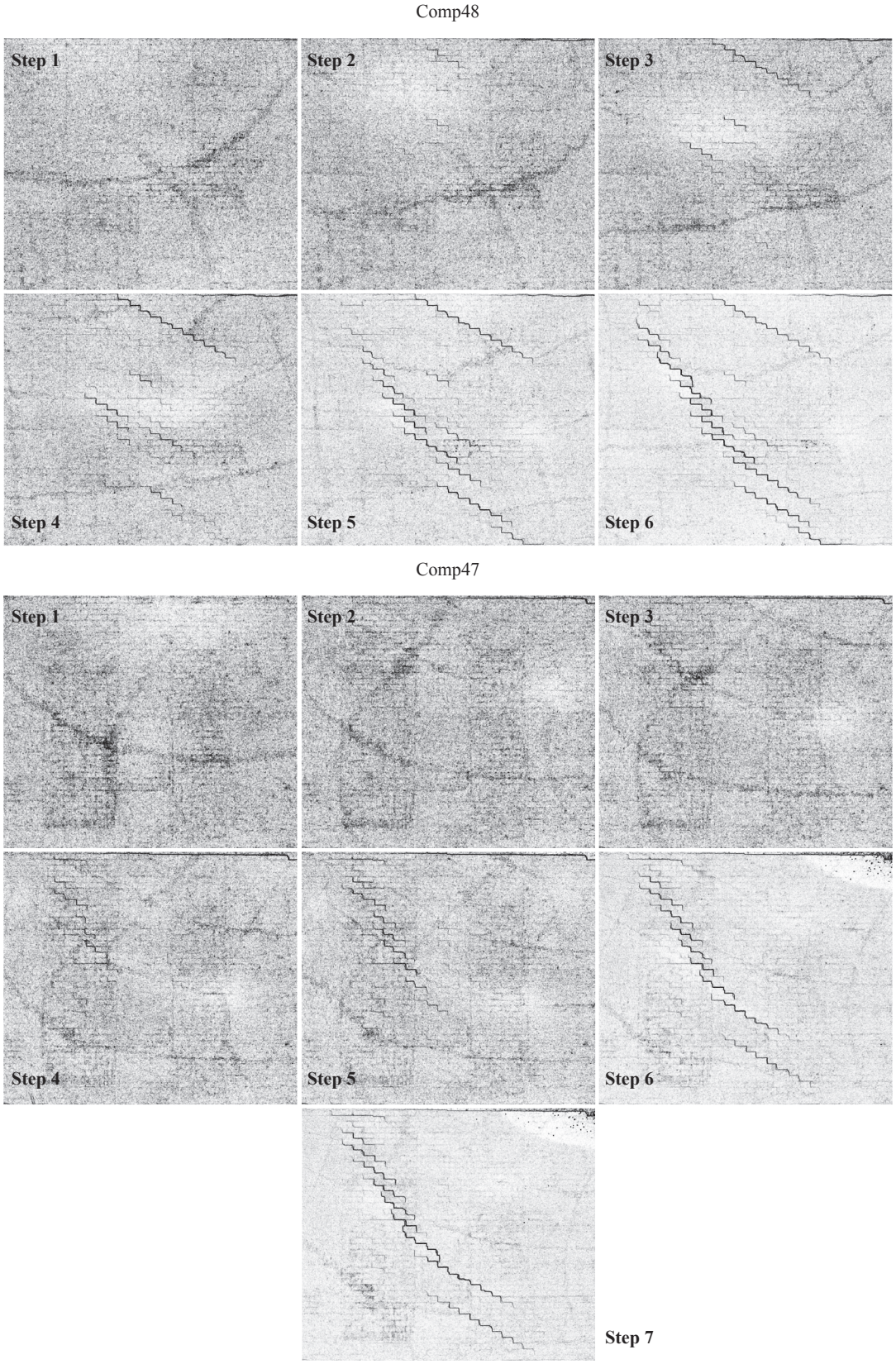

Fig. 6. Normalised principal strain from DIC displacement field showing localisation of strains for both walls at the moment of maximum positive drift towards the end of each step.

slipping open. In fact, the loading amplitudes in the negative direction do not trigger any crack directly attributable to them even though the base force reaches similar values in the positive and negative directions towards the end of the test (see Fig. 4). Fig. 9 shows that the negative drift utilises the existing cracks and while it does produce some diagonal cracks in the cross direction opposite to the main body crack, these

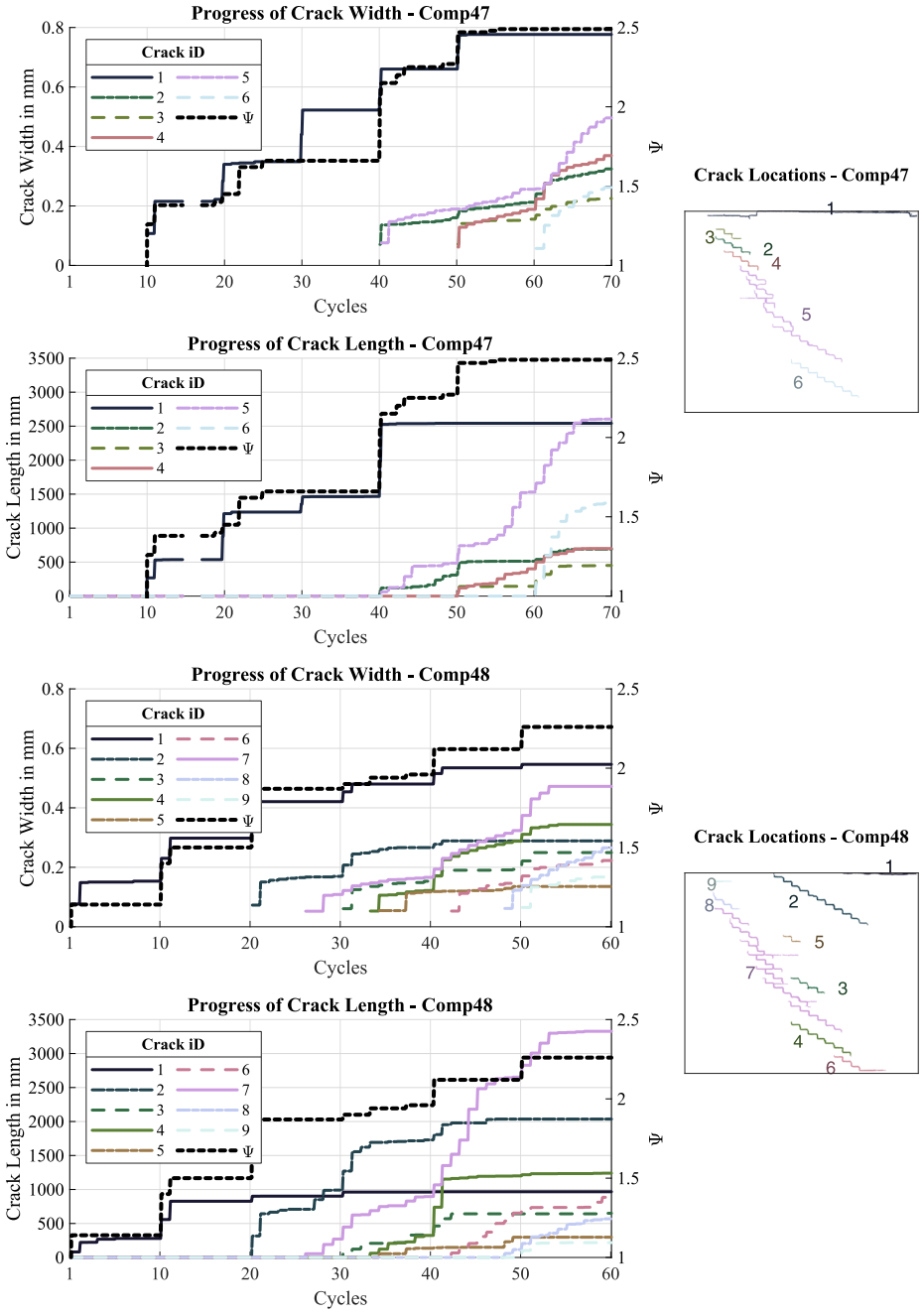

Fig. 7. Progression of crack width and crack length throughout the tests. Note that Ψ measuring the damage intensity of the entire wall is plotted as a dotted line and read on the right axis.

remain below the 0.1 mm threshold and are thus not shown in the summary of Fig. 7.

The lack of a bottom rocking crack is nonetheless not fully unexpected. In perfect shear deformation, only a body crack would be required, consisting of a diagonal stair-case crack developed fully from one side of the specimen to the other and allowing the entire drift to occur by sliding (and splitting) between the bricks; while, in perfect flexure (as could develop in a more slender pier), only two rocking cracks would suffice, and failure would ultimately occur as toe crushing. In this sense, the missing (anti)symmetry of the experiments corresponds to the imperfect boundary conditions and material properties which would never allow for perfect (anti)symmetry to occur. Early experiments by Cornelissen et al. [7] on direct tension of concrete prisms showed that, while the theoretical solution presented a crack propagating from both extremes to the centre of the prism, all experiments had a crack which predominated and propagated pass the centre to reach the other side of the prism. This was later explored numerically by Rots and de Borst [35] to be able to compute also the non-symmetric solution. Similarly, concrete beams (designed to fail in shear) will always present shear failure close to one of the supports even when shear forces are theoretically the same on both sides; any incipient crack on the non-failing side unloads [42]. Such cases of non-symmetry have been recently analysed numerically by Rots et al. [38]. In this light, the experiments of the shear wall with small drift values seem to correspond to a non-symmetric solution.

In terms of damage, both tests take place between $1 < \Psi < 3$ corresponding to the light damage range. The damage value follows mostly the increases in drift, but sees very small jumps as the cracks widen within a step. Fig. 10 displays damage against lateral in-plane drift and draws a linear fit for the values of positive drift, excluding

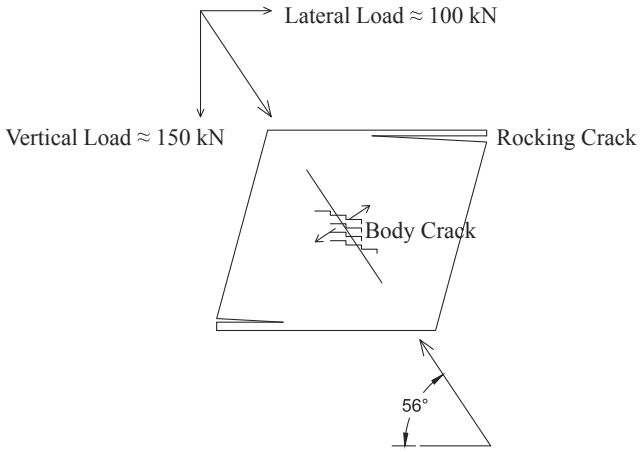

Fig. 8. Diagram of force flow and cracking lines towards the end of the test.

zero-damage. This figure also shows that the walls remain damaged (residual damage) for values of zero drift. Even for values of negative drift, the damage corresponds to that previously caused by the positive displacements. Contemplating the one-standard deviations of the Theil-Sen linear fit pegs light damage between a drift of 0.25‰ and 1‰.

The character of the light damage falls well within the categories defined by Petry and Beyer [34], where the drift behaviour of masonry (shear) walls is studied. Here, the first appearance of a vertical crack through a brick (along the diagonals) is marked as the start of "Limit State 2", or no longer light damage. This was observed in the tests herein only in the additional step (step 7), thus placing all previous steps in the regime of state 1. The limiting drift values for state 1 observed by Petry and Beyer [34,33] for their shear walls are also in the order of 0.1%. Furthermore, Godio et al. [16], who tested plastered stone masonry walls in two groups with a stark contrast in the number of cycles, concluded that while the capacity was not influenced by a larger number of cycles, the drift values at which to expect damage were extremely sensitive. Consequently, the aforementioned interval of 0.25–1‰ at which light damage can be expected, is most applicable for a large number of small cycles as tested in this study.

4. computational models

The full-scale walls described in the previous sections were modelled and analysed with the implicit finite-element software Diana FEA 10.3. Data of both experimental walls was used for the calibration and validation of the numerical models that are capable of reproducing the cracking behaviour of the masonry walls. The material characteristics were obtained from tests on smaller specimens. Moreover, two different modelling approaches were followed: a continuum macro-modelling and a micro-modelling. Where the former merges in one material the properties of brick and brick-mortar interface; in the latter, the two components are modelled separately. In the macro-models, the damage is spread in all elements (smeared), whereas in the micro-models, cracks localise in interface elements pre-placed at positions of joints and/or at the middle of bricks (see e.g. [37,25]), or in continuum elements used for mortar joints.

First, Section 4.1 presents the model of experimental walls, calibrated and validated with the macro-modelling approach. Then, in Section 4.2, the same walls are analysed with the micro-model.

4.1. Calibration of macro-model

The in-plane, full-scale, baked-clay masonry wall was modelled with 2D plane stress elements. The model was 3050 mm wide, 2700 mm high and 100 mm thick. Both top HEB-600 and bottom HEB-300 steel beams were modelled as elastic line beam elements (CL9BE). As during the experiments, a vertical pre-compression of 0.46 MPa was applied as a line load on the top beam, and double clamped boundaries were assigned to the model by fully fixing the bottom beam and by constraining the in-plane rotation of the top beam. In addition, equal rigid ties are applied to the vertical DoFs of the top beam such that the top edge may only move rigidly in the vertical direction. The in-plane drift was then applied in displacement control at the left node of the top beam. As element typology, quadrilateral 8-node quadratic elements (CQ16M) were employed for the masonry wall with a mesh size of 50 mm considering a full 3 × 3 Gauss integration scheme. A view of the model mesh is shown in Fig. 11.

The steel material of the beams was kept linear (ρ = 7.85 ton/m^3, E = 210 GPa, ν = 0.3), and a non-linear material model was used to properly simulate the cracking behaviour of masonry. An orthotropic total-strain based masonry model (also called Engineering Masonry Model – EMM in Diana) was selected as constitutive model [36,41]. This model includes different values of inelastic and elastic properties for the two main directions: the local × parallel to bed-joints and local y aligned with the head-joints. The in-plane crack directions are four: two of them are located along the joints axis and the other two are diagonal, taking into account the masonry pattern by a parameter (predefined angle for diagonal cracking). As failure mechanisms, the material model includes tensile cracking with softening and secant nonlinear unloading/reloading behaviour, Coulomb friction with cohesion softening and elastic unloading/reloading, and compression crushing (in both horizontal and vertical directions) with mixed secant/elastic unloading and reloading behaviour. Multiple options for the head-joint failure can be considered in the material model. For the

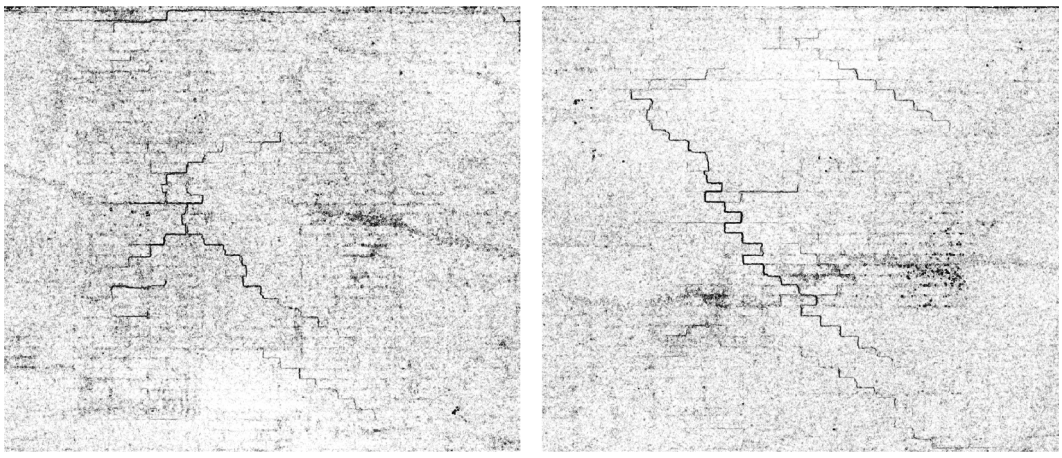

Fig. 9. Normalised principal strain from DIC at maximum negative drift towards the end of the test for Comp47, left, and Comp48, right.

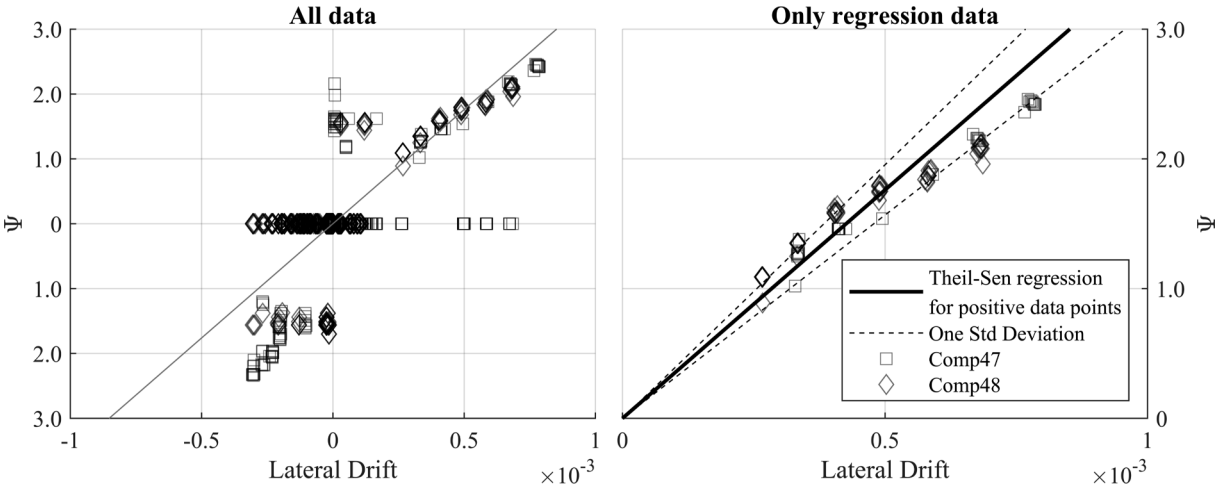

Fig. 10. Damage parameter Ψ against lateral, in-plane drift. Left, showing all data points; and right, showing only non-zero, positive data points used for a linear slope regression. The regression line is also drawn left for reference purposes.

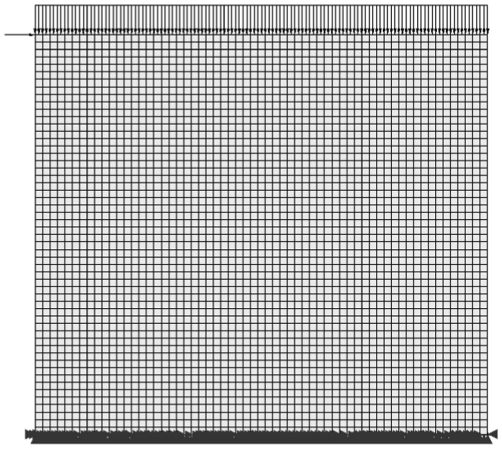

Fig. 11. Finite element model of Comp47-48 using a quadrilateral mesh.

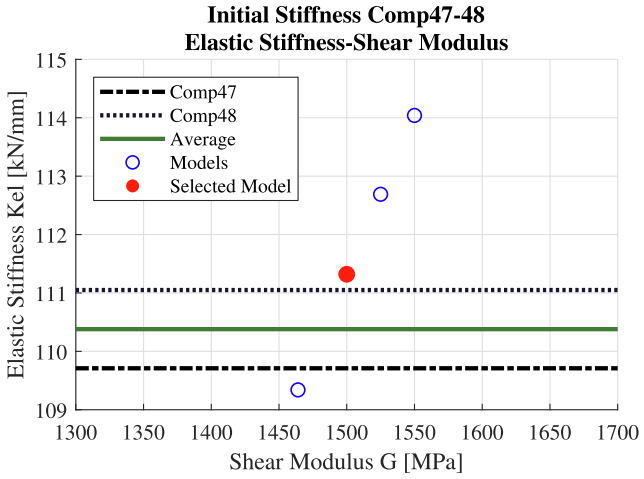

Fig. 12. Calibration of initial stiffness of Comp47-48 varying the G modulus of macro-model.

calibration model, the "Friction based" option was selected. In this case, the tensile strength of the head-joint is calculated from the friction shear-stress in the bed-joint, though a minimum value of tensile strength in the head-joint must be provided. For robustness and simplicity, the Poisson's ratio of the model was set to zero; this has an influence on the elastic behaviour of the model (see for example [48]), but since the focus of this study is on the non-linear behaviour (cracking) of the material, where Poisson's ratio effectively diminishes to zero during softening, and for which the orthotropic EMM does link the two directions as discussed above, the assumption has been considered valid.

The material properties were partially selected from small companion tests such as bond-wrench tests, compression wallets, shear triplets and in-plane bending tests, and partially from the actual wall data. The calibrated values were varied within two standard deviations of the companion tests to assess their influence, but selected within one standard deviation to ensure a realistic set of properties. For example, the direct tensile strength, which is key for accurately determining the rocking and diagonal cracking behaviour, was varied between 0.1 and 0.2 MPa, ultimately selecting 0.16 MPa corresponding to the upper one standard deviation value from small scale tests. Additionally, the cohesion and friction angle, paramount in describing the behaviour of shear walls, are directly linked to a higher capacity and inversely proportional to the energy dissipation. The cohesion was studied in the range of 0.13–0.26 MPa with 0.17 MPa being the value selected; while the friction angle was observed within 0.68–0.71 rad. As a final example: the shear modulus G, which influences the initial stiffness of the shear walls, was calibrated in order to consider the wall stiffness of experiments Comp47-48 but also other similar clay specimens of the same campaign (not presented here, see [21] as these were all built of the same material. The variations of G, having been studied in the range of 1450–1550 MPa, is shown in Fig. 12 with the selected value as a solid

Table 1
Material properties of macro-model. *(1-Tested Value, 2-Estimated Value, 3-Computed value)*.

Material Properties	Clay Masonry	
Density	1624 kg/m^3	*1*
Elastic Modulus Perpendicular to Bed-Joints	3 571 MPa	*1*
Elastic Modulus Parallel to Bed-Joints	2 497 MPa	*1*
Elastic Shear Modulus	1 500 MPa	*2*
Bed-Joint Tensile Strength	0.16 MPa	*1*
Minimum Head-Joint Tensile Strength	0.16 MPa	*2*
Tensile Fracture Energy	11.30 N/m	*3*
Vertical/Horizontal Compressive Strength	12.93 MPa	*1*
Vertical/Horizontal Compressive Fracture Energy	35 590 N/m	*1*
Friction Angle (Friction Coefficient)	0.688 rad (0.82)	*1*
Cohesion	0.17 MPa	*1*
Shear Fracture Energy	209 N/m	*1*
Head Joint Failure Option	Friction Based	
Predefined Angle for Diagonal Cracking	0.50 rad	*1*

Table 2
Analysis phases properties of macro-model of Comp47-48.

Analysis Phases	Applied Load Case	Load Step	Iterative Method	Norms	Tolerance
Phase 1	Gravity Load + Overburden	10% load/step	Secant BFGS (Quasi-Newton)	Force & Displacement	10^{-3}
Phase 2	Lateral Displacement	0.01 mm/step		Force & Energy	10^{-2} & 10^{-3}

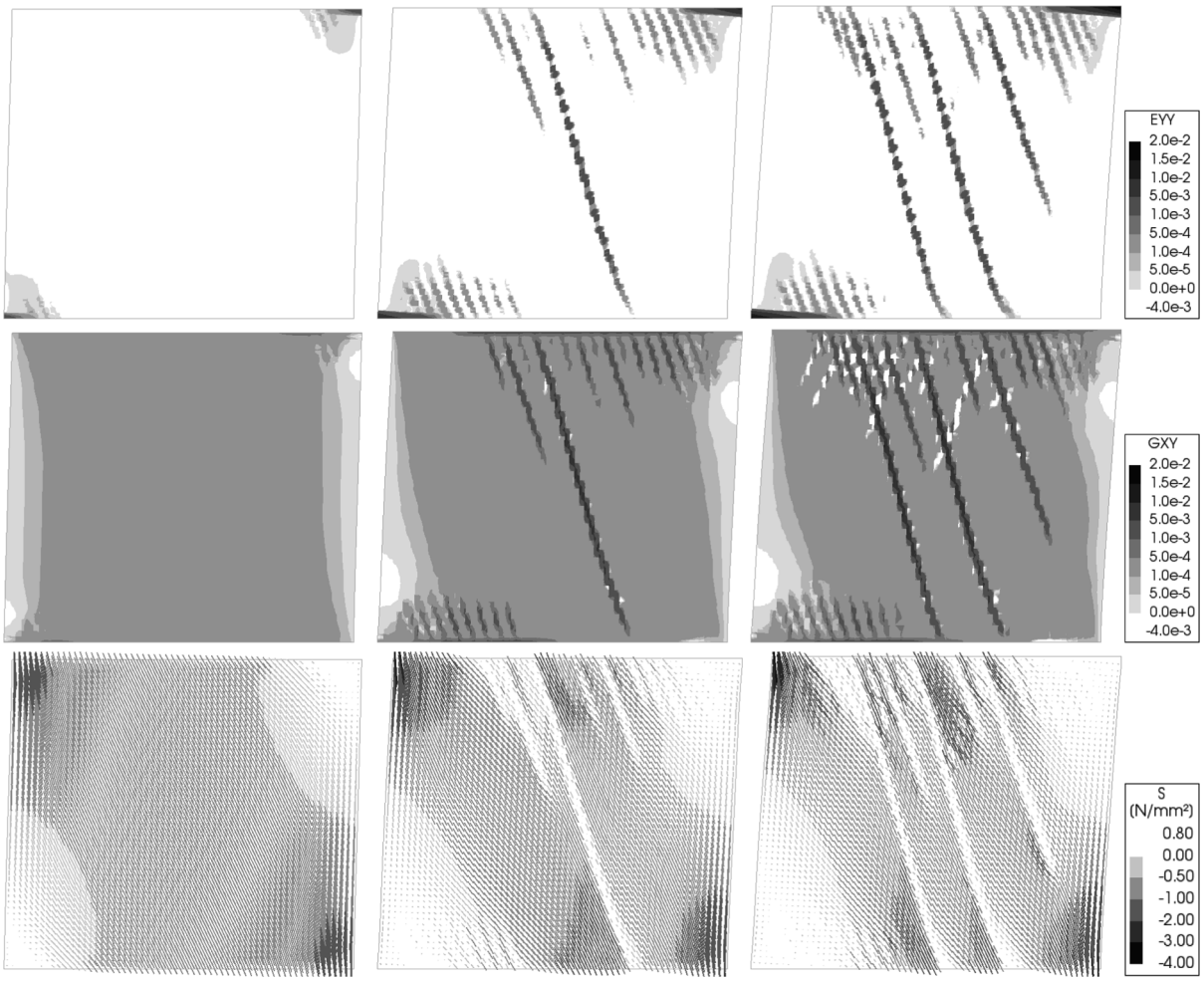

Fig. 13. Contour and tensor plots of macro model at maximum positive peaks of different steps, from left to right: first step (drift 0.26‰), fourth step (drift 0.49‰), last step (drift 0.67‰). Plots of, from top to bottom: vertical strain contour, shear strain contour, principal stress tensors. Deformed magnitude: ×100.

dot. The average stiffness of the shear walls 47–48 was 110.4 kN/mm and the model with the selected value exhibits a lateral stiffness of 111.3 kN/mm. A list of the material properties employed for the baked-clay masonry is shown in Table 1.

Two phases were used in the model. In the first one, gravity and overburden were applied, and the displacement field, yet not the stress field, was cleared after this phase. In the second phase, the in-plane, displacement-controlled load was introduced in the model. The experimental protocol was employed (see Fig. 3), but, in order to optimise the computational time, only three of the ten cycles per step were considered. The load steps, iterative method, norms, and absolute tolerances adopted during the two phases of the analyses are summarised in Table 2. Both material and geometrical non-linearities were taken into account. For the entire analyses, the Parallel Direct Sparse method was used to solved the set of equations.

The strain-stress evolution of the model is depicted in Fig. 13. In this graph, vertical strain, shear strain and principal stress tensors at three different drift amplitudes are shown. When the first peak is reached, at a drift of 0.26‰, two rocking cracks appear at opposite corners, where the positive stress reaches the bed-joint tensile strength. The cracks appear (anti)symmetric. No unloading of neither of them is detected, thus a potential bifurcation or lowest equilibrium path may be missed, as the global stiffness matrix is based on local secant stiffness. If it was based on local tangent (negative softening), it would be possible to detect a stiffness bifurcation, introduced for instance, via local imperfections and thus steering the solution to the non-symmetric lowest equilibrium path [35,38]. This is however not implemented in this study and an antisymmetric initial failure is presented by the model. The problem of mesh objectivity, also called mesh directional bias and mesh size bias, is still an open topic in the computational mechanics field (e.g. [39]). In addition, the constant strain formulation of the elements allows smoother crack localisation. One of the solutions to overcome the problem mentioned above, could be to use a smeared constitutive crack model with a local crack-tracking algorithm as suggested for instance by Pelà et al. (2014) or Slobbe et al. [42].

Both experiments also highlight rocking cracks as initial failure. During this phase, shear deformation is constant in the middle part of the wall and does not exceed the failure point (Fig. 13). Compression

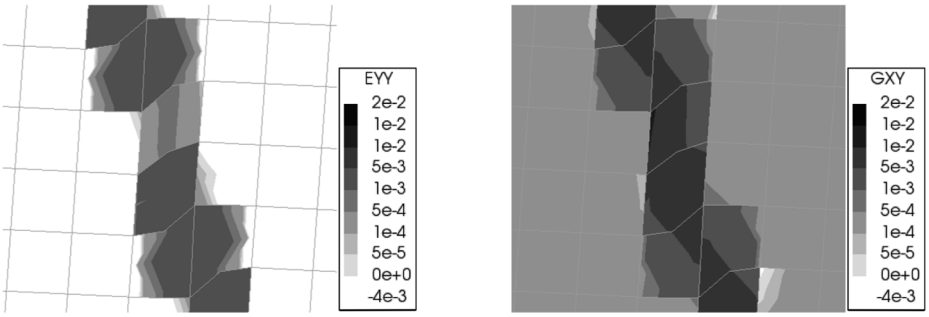

Fig. 14. Magnification of mid diagonal crack at drift of 0.67‰. Contour plot of (left) vertical strain and (right) shear strain. Deformed magnitude: ×100.

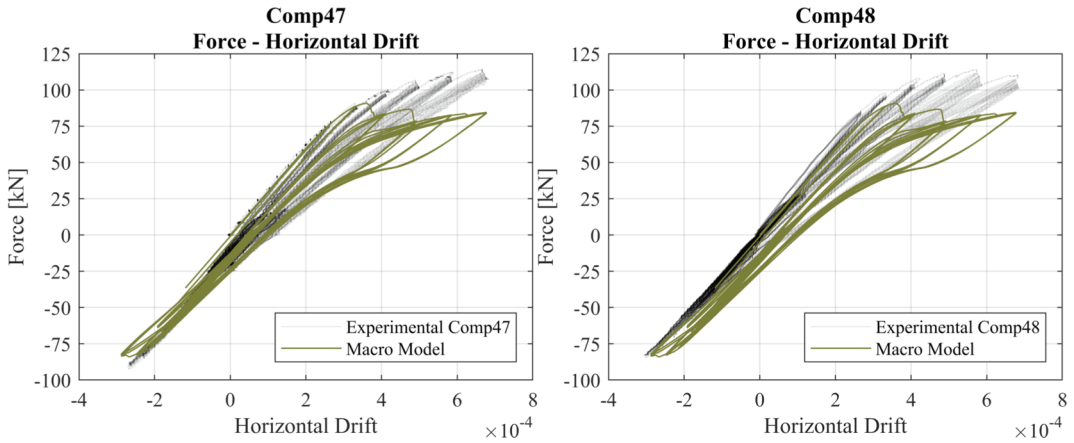

Fig. 15. Force-drifts comparing FE macro model and experimental walls Comp47 (left) and Comp48 (right). Note that the model is identical in both graphs and the experiments vary.

stresses follow the diagonal strut in a regular manner without considerable deviations. Diagonal cracks start to develop when approaching a drift value of 0.49‰. Minor shear cracks then emerge close to the corners where rocking cracks are already present. The main diagonal crack runs from top to bottom of the wall with an angle of about 74° (measured against the horizontal base line). At this point of the protocol, the tensors of principal stresses in Fig. 13 reveal a net division between left and right part of the wall, in which both sides are carrying the vertical load; the lateral force of the model undergoes a sudden reduction (Fig. 15). The damage pattern of the model after the first cycle of the fourth step is slightly overestimated in respect to the experiments which only show the top rocking crack and minor shear cracking. At the last cycle (drift of 0.67‰) a second shear crack, triggered already in the fifth step, is fully visible on the mid-left side of the model running from top to bottom. In addition, a third shear crack located at the top-right part extends downwards to the mid-height of the wall. A zoom of the mid diagonal crack of the model is presented in Fig. 14 where the crack is expressed in terms of vertical and shear strain. Here, the deformed mesh clearly shows a slip between two vertical bands due to the lateral deformation and double clamped boundary conditions. The resulting failure mechanism is a combination of shearing boosted by vertical extension, with horizontal strains appearing to be negligible. Shear cracks, formed during previous negative drifts, can be detected by the plastic negative shear strains depicted in white in Fig. 13. The force transfers from top to bottom through three clear compression bands, with a maximum value of compression at the toe equal to 3.2 MPa, much lower than the masonry compressive strength. Thus, no crushing was detected, in accordance with the experiments.

The plot of force against horizontal drift produced by the model is compared to each of the experiments in Fig. 15. The capacities of Comp47 and Comp48 are respectively 114.1 and 113.8 kN in the positive direction and −92.3 kN and −84.5 kN in the negative direction. The maximum lateral force of the model is underestimated for positive drift (91.0 kN) while it is in good agreement with both specimens in the negative side (−84.0 kN). As aforementioned, the two visible drops in capacity are strictly correlated with the two subsequent diagonal cracks. Some hysteresis develops along with shear cracking and it is also in line with the experiments. During the last cycles, the severe shear damage produces a slight overestimation of the energy dissipation. Yet, an improvement can be seen in the simulation of energy dissipation in comparison to a standard isotropic (concrete-like) total-strain based model with secant unloading-reloading curves, as frequently used for masonry by e.g. Lourenço et al. [26], Giardina et al. [15] and others, which strongly underestimate the energy dissipation under cyclic loading condition [36,41]. The force degradation of the model is underestimated for both positive and negative peaks as is expected from the reduced number of cycles in the models and lack of material degradation at the material model scale, with values in the order of 1% against the experimental 10%. The strength degradation, not yet implemented in the material model, could be added in future improvements in a fashion similar to Bindiganavile-Ramadas [3]. As in the tests, the reduction in strength is initially bigger and reduce when approaching the last cycle in a step. In terms of damage, Fig. 16 depicts the cumulated crack pattern of the first peak of step four and at the end of the protocol. The model gives a damage value (Ψ) of 1.8 while experiments show 1.7 and 1.9 (Ψ for Comp47 and 48, respectively). Similarly, the final crack pattern of the model looks in reasonable agreement with the tests. The computed Ψ at the end of the protocol of Comp47 is 2.6 and of Comp48, 2.3, while the model provides a value of 2.2. These values were determined with a purposely-written program. For consistency, the crack data from the DIANA models (maximum crack width from the Engineering Masonry material model, EMM) was extracted at every integration point and treated as if it were

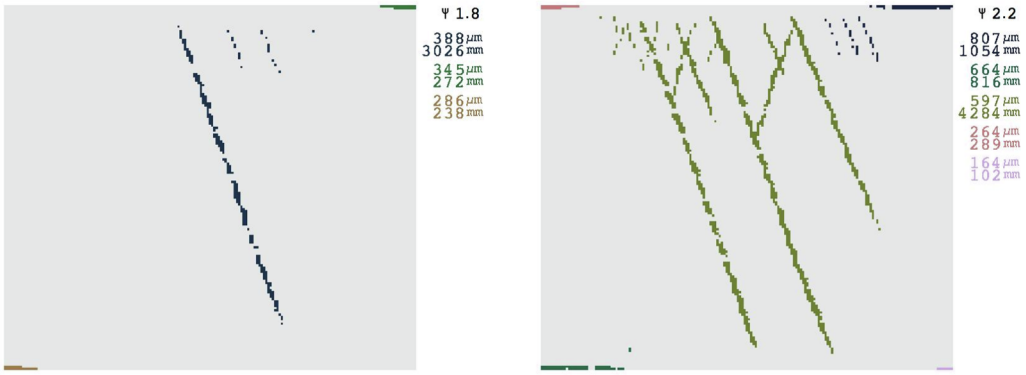

Fig. 16. Cumulated crack pattern and Psi value (Ψ) of model at (left) first peak of step four and (right) end of protocol.

experimental DIC data where a program identifies crack openings over a specifiable threshold (of 0.1 mm), and groups neighbouring, cracked points together into discrete cracks (at a minimum length of 100 mm). Finally, each crack was identified with its length and a maximum crack width, which together with the number of cracks in a wall allowed for the computation of Ψ as per Eq. (1).

Regarding the sensitivity of the model, considering the same initial stiffness conditions, the value of cohesion and friction coefficient have a great impact on the results in terms of force and hysteresis. Although an increment of these two parameters showed a better match between experiments and numerical model, their increase exceeded the limits found by small material tests and hence, would have been an unrealistic choice. The tensile strength properties mainly affect the point of crack initiation/propagation of rocking cracks. Looking at the convergence of the analysis, 0.47% of the total steps did not converge. These steps were detected during large increases in cracking and force reduction, yet the correct solution path was quickly recovered after these no-convergence points.

4.2. Calibration of micro-model

The experimental squat wall was also analysed with a micro-modelling approach. Here, bricks and mortar were modelled as separate components: a linear material was used to model the bricks since they did not show non-linearities in the serviceability limit state of the 'light damage' experiments; and, the non-linearities are included in head- and bed-joints which were modelled as a single layer of continuum elements using the orthotropic, total-strain-based masonry model as constitutive law [36,41]. In fact, that model, intended for use of masonry as a composite, was purposely 'misused' here to model individual joints because of its features of distinguishing between tensile, shear, compression and dedicated unloading/reloading for these modes. An overview of the micro-modelling approach is given in Fig. 17. It must be noted that interface elements between mortar and brick are not used in this micro-model; the approach makes use of continuum elements only. Following this methodology, the full scale wall was modelled in 2D with plane stress elements. The wall dimensions are 3070 × 2700 × 100 mm with boundaries, loads and beam elements kept equal to the macro-model. Similarly, the same quadratic-order quadrilateral elements used in the macro-model are employed (CQ16M), with a Gauss 2 × 2 integration scheme and a mesh size of 10 × 10 mm. A 2D view of the model is shown in Fig. 17.

Since the elastic modulus of the mortar was not evaluated in the small companion tests, it was calibrated from the initial stiffness of the in-plane clay walls by keeping the assayed properties of the bricks constant (ρ = 1.624 ton/m^3, E = 8049 MPa, ν = 0.16). The elastic modulus of the head joint was halved with respect to the bed joint one whereas the shear modulus of the mortar was computed as G = E/(2 + 2ν). The rest of the properties were maintained between the two different joint types; Table 3 summarises the mortar joint parameters. The experimental loading protocol of Fig. 3 was reduced to one cycle per step and the same analysis settings of the macro-model were kept, except for the load step that was increased from 0.01 mm/step to 0.05 mm/step to reduce the computational time without significantly affecting the model results. Note that Psi was not computed for the micro-models.

The detected damage mechanism at the main positive peak of the last step (drift of 0.67‰) is depicted in Fig. 18, where principal tensile strain tensors highlight two flexural cracks at the bottom left side and at the top right side along with a middle, localised, diagonal body crack. The latter, at the mid height of the wall, is illustrated more in depth via three strain components (Fig. 18, right). The deformed view shows the local mechanism to which joints are subjected to. Differently from the continuum macro-model where vertical and shear strain components

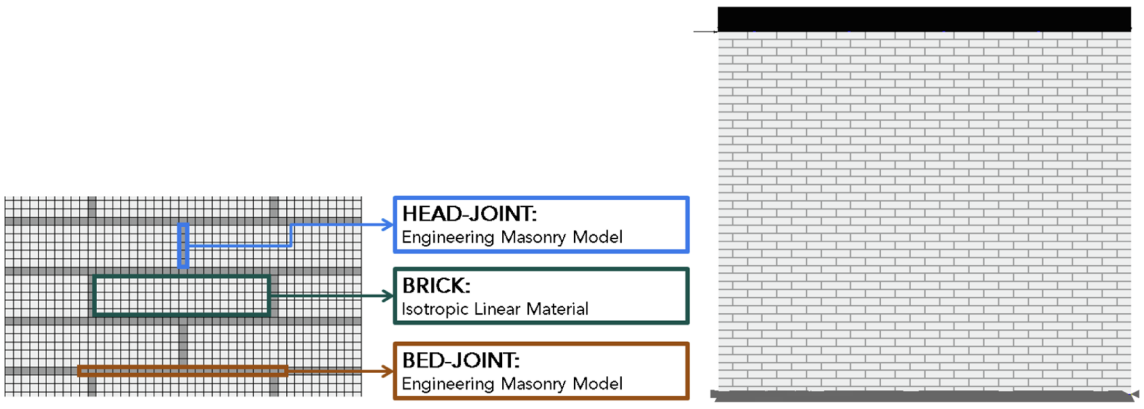

Fig. 17. Finite element micro-model of Comp47-48. Modelling approach (left) and 2D model (right).

Table 3
Material properties of micro-model. *(1-Tested Value, 2-Estimated Value, 3-Computed value).*

Material Properties	Mortar Bed Joints	Mortar Head Joints	
Density	1624 kg/m^3		*1*
Elastic Modulus of Masonry Joints	1050 MPa	525 MPa	*2*
Elastic Shear Modulus of Masonry Joints	453 MPa	226 MPa	*3*
Masonry Joints Tensile Strength	0.08 MPa		*1*
Tensile Fracture Energy	6.9 N/m		*3*
Compressive Strength	3.59 MPa		*1*
Compressive Fracture Energy	6.4 N/m		*2*
Friction angle (Friction coefficient)	0.688 rad (0.82)		*1*
Cohesion	0.13 MPa		*1*
Head Joint Failure Option	Direct input Head Joint		
Shear Fracture Energy	300 N/m		*1*

were predominant along the diagonal cracks, the presence of stiff linear bricks in the micro model modifies the damage picture. Mid head joints stretch in the horizontal direction showing a high horizontal strain, while bed joints are mainly subjected to shear failure; the vertical strain is lower than the other two components. In contrast to the macro-model, where the main shear cracks start from the top downward, in this modelling approach the shear cracking initiates in a few head-joints in the central part of the wall, more alike the experiments. From step four onward, the body crack propagates stair-step-wise along the two diagonal directions. The second experimental wall, Comp48, exhibited a similar behaviour regarding the mid diagonal crack. The force-drift curve of the model is then compared against the curves of the experimental specimens. As can be seen in Fig. 19, the initial and final stiffness are in line with the experiments (especially for Comp47), and the capacity at the positive side is in good agreement with both tests. The maximum positive lateral force of the micro-model is 103.8 kN while at the negative side the results are slightly overestimated. The large shear strains associated with the middle crack implies an overestimation of the energy dissipation after step four; this excess is also visible at zero drift where the residual force reaches −50 kN. In general, the wall micro-model is able to simulate well both the capacity and the crack pattern of the tests while overestimating the dissipation of energy. Regarding the analysis convergence, 13 out of 670 steps (1.94%) did not converge for the micro-model, but convergence was then rapidly regained in subsequent steps. Additionally, the computational time of micro-model simulating one repetition per step was two times higher than the macro-models, where three cycles were included per step.

5. comparison against ground motion signal

The macro-model of the full-scale walls, calibrated in Section 4.1, is adopted in this section for NLTHAs, since, although the micro-model showed a better agreement with capacity and crack pattern than the macro-model, its use for dynamic analyses would lead to a high computational time. In Section 4 the outcome of the shear wall subjected to quasi-static loading was presented. Conversely, in this chapter, its exposure to single or multiple earthquake excitations at its base is reported. This is thus an extrapolation study upon the calibrated models. In a further extrapolation, two different materials are employed: a standard masonry and a poor masonry which considers a set of reduced properties. First in Section 5.1, the description of the model for the dynamic analyses is discussed. Then, in Section 5.2, the results and the extrapolative framework are obtained.

5.1. Model for non-linear time-history analyses

The macro-model, presented and discussed in Section 4.1, was set-up for dynamic analyses using a quadrilateral mesh. In respect to the models described in Section 4.1, some adjustments were included in the models for the NLTHAs:

- Additional poorer material: the elastic properties are 1.3 times lower than the calibrated values: tensile strength and cohesion are reduced by 30%. Tensile and shear fracture energy are reduced by keeping a parallel slope in the post-peak softening branches (Fig. 20). This

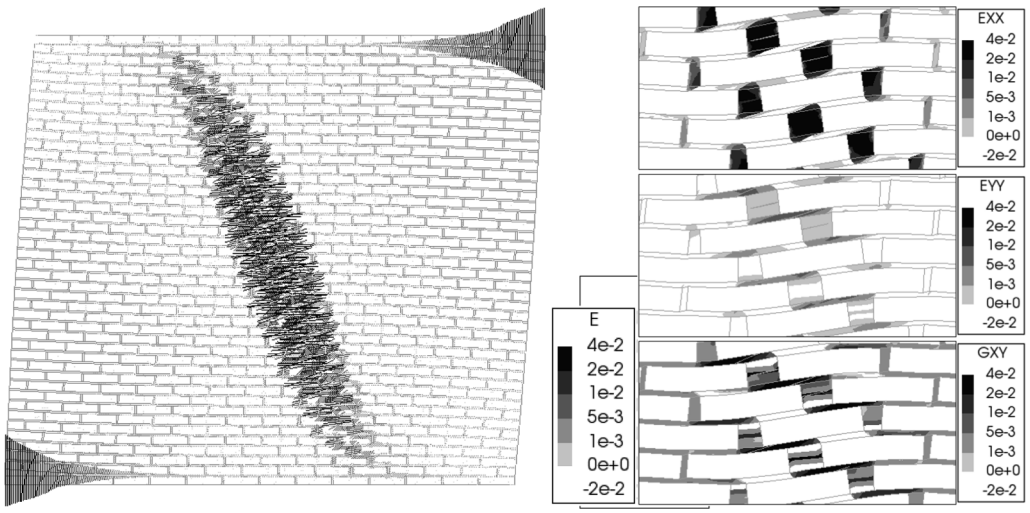

Fig. 18. Principal tensile strain tensors (left) and strain components (horizontal, vertical, and shear) of centre of model (right) at the positive peak of the last step (drift 0.67‰). Deformation magnified ×100 (left) and ×200 times (right).

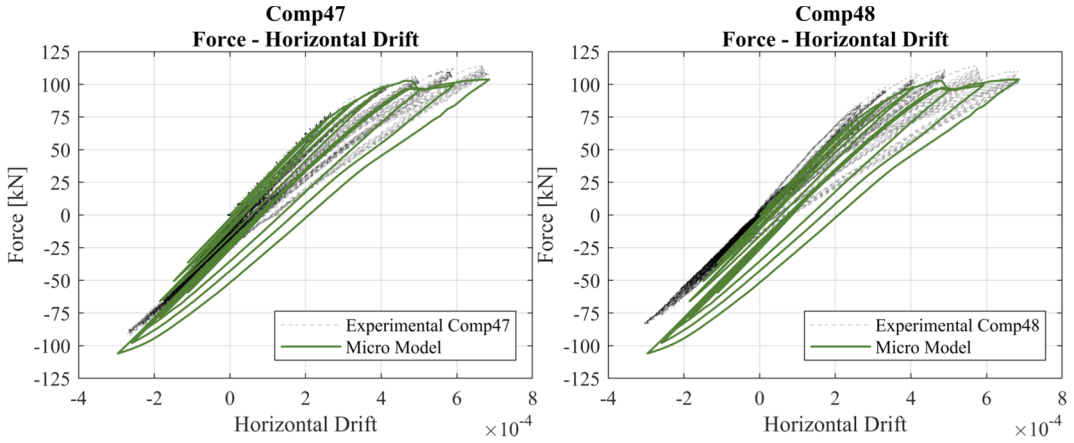

Fig. 19. Force-Drifts plots comparing micro FE model and experimental walls Comp47 (left) and Comp48 (right).

implies that the fracture energies are reduced by more than 30% and correspond to 49% (0.7 × 0.7) of the original fracture energy.

- Top and lateral boundaries: top and bottom steel beams are removed. The top boundary is replaced by a line mass element representing the dynamic effect of an upper mass constituted by a floor and a roof with a value of 10 ton. Then, the natural period of the wall corresponds to 0.079 s for the model with standard material and 0.089 s for the model with poor material (13 Hz and 11 Hz, respectively). The static condition is not influenced by the mass element. Besides the masonry gravity load, the pre-compression is provided by a vertical overburden of 0.12 MPa which acts on the top edge of the wall. To simulate the constraints of transversal walls, two vertical linear beam elements are attached to the lateral edges. A fictitious cross-section of one brick is given to the elements, including a mass that represents the out-of-plane contribution of a wall of 3 m in length along the transversal direction.
- Soil-Structure Interaction: a combination of springs and dashpots is placed at the bottom edge of the wall in order to simulate the effect of a sandy soil underneath the structure. A non-linear Coulomb friction law (cohesion equal to 0.1 MPa, friction and dilatancy angle equal to 0.61 rad) is adopted for the springs. Stiffness and damping parameters are evaluated according to the Gazetas formulations (NEHRP, 2012) and discussed in Van Staalduinen et al. [47]. The vertical stiffness modulus is set to 0.435 N/mm^3 underneath the middle part of the wall and to 0.565 N/mm^3 beneath the lateral side of the wall. The horizontal stiffness is 0.376 N/mm^3. The vertical damping coefficient is 205.6 Ns/mm and 6.862 Ns/mm underneath the middle and the lateral part of the wall, respectively. The horizontal damping coefficient is set to 109.9 Ns/mm.
- Rayleigh Damping: a damping of 2% based on the first two modes (for participating mass) is included in the model.
- Input: a 'near-field' record of the Zeerijp earthquake (registered on the 8 of January of 2018 at the Garsthuizen station) is applied as imposed acceleration at the base of the model. Both horizontal and vertical components are employed in the model. The original signal, with a peak ground acceleration (PGA) of 0.11 g is depicted in Fig. 21. This motion corresponds to a peak ground velocity (PGV) of approximately 30 mm/s. In addition to the original signal, amplified motions of 60 and 120 mm/s are investigated (with arbitrary amplification factors of 2 and 4). To include the effects of the repetitions, the motion is applied in sequence, multiple times. Three scenarios of a series of one, two and four earthquakes of equal amplitude (PGV) are examined.

5.2. Extrapolation and results of dynamic analyses

A set of eighteen NLTHAs was investigated and compared. The finite element model employed for these analyses was discussed in the previous section. The analysis procedure was divided in two phases: during the first one, gravity and overburden loading were introduced in the model; then, in the second phase, the base motion was applied. The main model parameters are as follows: a time step of 2 ms is used to discretise the total length of the motion (equal to 12.62 s for a single earthquake); physical and geometrical non-linearities were considered in the model; the Newmark-Beta ($\beta = 0.25$, $\gamma = 0.50$) was employed as time integration method; consistent mass and damping matrices were used in the calculation; secant (Quasi-Newton) BFGS was employed as iterative method; line search was activated during the analyses; energy norm with an absolute tolerance of 0.001 was selected; and, the system of equations was solved using the Parallel Direct Sparse method. From

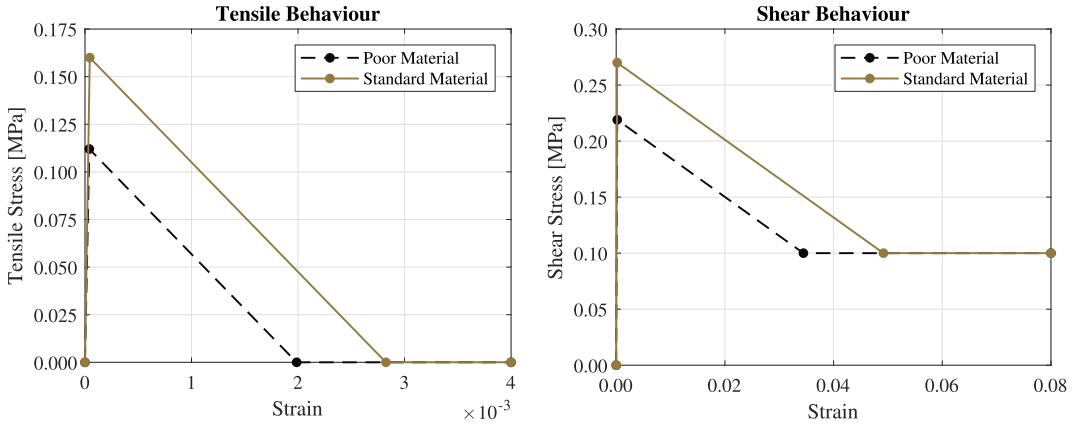

Fig. 20. Constitutive laws for the two different materials. Tensile (left) and shear considering 0.1 MPa pre- compression (right).

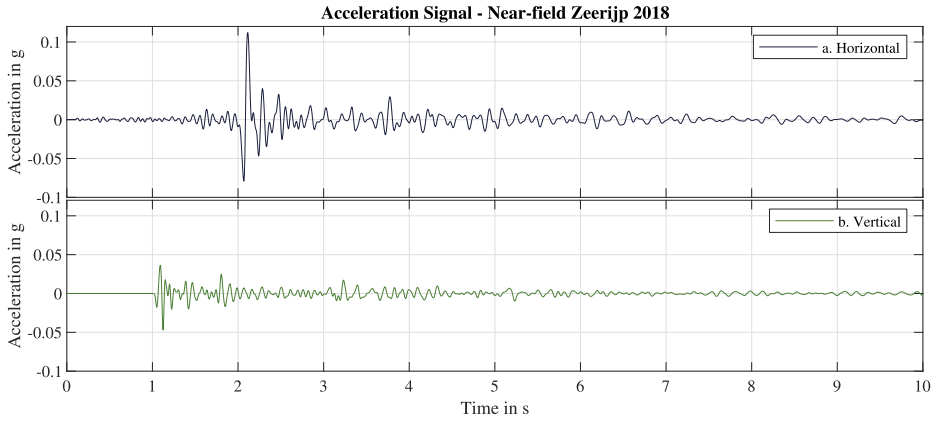

Fig. 21. Near-field Zeerijp (2018) earthquake signal, (a) horizontal and (b) vertical acceleration plot.

the models, the maximum cumulated principal crack width recorded up to the end of the loading protocol was extracted. The post-processing was fully automated so as to guarantee an objective comparison; the results were processed in the same way as the experimental DIC data. Both shear and opening cracks were accounted for in the computation of the final damage value Ψ.

An overview of the entire set of NLTH analyses is summarised in Table 4. Here, the maximum damage encountered during the entire motion is presented. The analyses show no damage for the lowest PGV (30 mm/s, 1× the maximum registered) and standard masonry. Damage values greater than $\Psi > 1$ are identified for most of the cases with standard masonry and motion amplification factor 2×. Similar values are detected for poor masonry already at 30 mm/s of PGV; while large values of light damage ($\Psi > 1.5$) are discovered for a PGV of 120 mm/s (3 times the registered value), especially for poor masonry. Damage values above 2.0 are detected after 4 earthquakes with a PGV amplification factor of 4×. Following the trend provided by the results, light damage ($\Psi > 1.0$) of standard masonry is triggered by a single earthquake of approximately 55 mm/s. Such values are then strongly reduced when multiple earthquakes act sequentially. The value drops to 45 mm/s after 4 earthquakes in a row. The accumulation of damage provided by multiple subsequent motions is in some cases very relevant as it can reach an increment in damage of up to 52% when comparing the cases with one and four earthquakes of 120 mm/s (standard masonry). A comparison of the damage pattern between three cases of poor masonry is given in Fig. 22.

6. Conclusions

This article presents the implementation of high-resolution Digital Image Correlation to measure the displacement field of squat walls of clay-brick masonry tested in a double-clamped configuration. The experiments focused on the repetition of very low values of lateral, in-plane drift (up to 0.1%) to observe the initiation and propagation of cracks, characteristic of the aesthetic or light damage state for frequent gas-extraction-induced earthquakes. The DIC was successful in monitoring the progression of the cracks to show an increase in crack width not only when the drift applied grew in amplitude, but also when the same amplitude was enforced repeatedly. Non-symmetric rocking cracks at the edges of the walls propagated horizontally while diagonal body cracks, characteristic of shear behaviour, initiated around the centre of the walls and propagated outwards diagonally following the joint patterns of the masonry. The body cracks consisted initially of parallel diagonal stair-case patterns, but localised into a single wider crack as the experiments progressed. The experiments showed that for these types of walls, light, aesthetic damage can be expected to take place between 0.25‰ and 1‰ of in-plane lateral drift when multiple cycles are considered.

The localisation of cracks had been seen in early computational models twenty years ago but had not been observed experimentally due mainly to the lack of resolution in the monitoring techniques and focus of experiments on larger drift values. The more detailed finite element models calibrated herein also displayed this behaviour while accurately representing the force-displacement relationship of the walls and their crack patterns. Both macro- and micro-modelling approaches showed good agreement with the experiments. Micro-models very promising in terms of results but were time consuming. While sensitivity analyses with a macro-model revealed some bias related to mesh size and direction. The calibrated macro model with quadrilateral mesh was then used to elaborate a series of time-history analyses of a ground motion signal applied with its original acceleration and magnified two and four times. The models showed that at its original acceleration corresponding to a peak ground velocity of approximately 30 mm/s, the seismic motion caused undetectable, incipient damage below the threshold set for light damage. A repetition of the ground motion on the same, now damaged model, then increased the damage to just over the

Table 4
Summary of analyses results in terms of damage values Ψ.

Ψ		Poor Masonry			Standard Masonry			Number of Earthquakes	Legend
		1x	2x	4x	1x	2x	4x		
Quadrilateral Mesh	1x								0
	2x								0.5
	4x								1.0
Amplification Factor									1.5
									2.0
									2.5

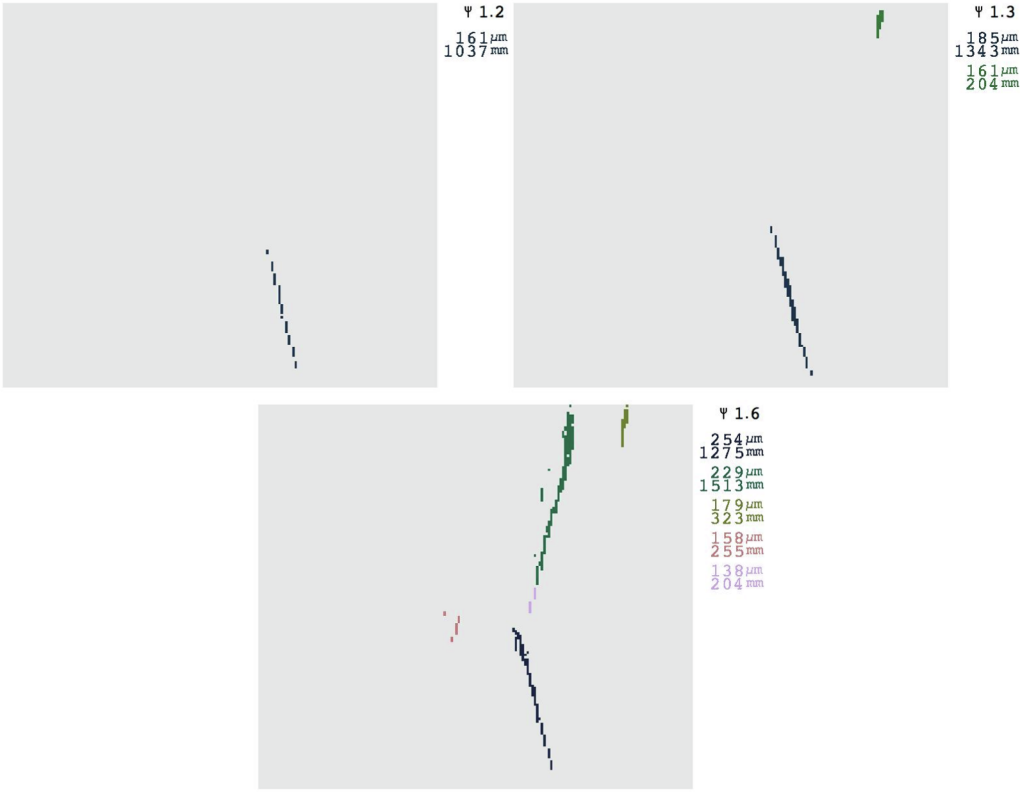

Fig. 22. Damage pattern in terms of Ψ for poor masonry, PGV of 60 mm/s for one (top left), two (top right) and four (bottom) earthquakes in series.

lower boundary set for light damage, thus making it detectable. A four-fold increase in the intensity of the ground motion was necessary to reach the upper boundary of light damage, with a 50% increase in damage when three additional repetitions of the ground motion were applied.

In sum, the rigid, squat brick-masonry walls tested experimentally in shear display a reduced drift capacity to light damage in comparison to walls tested with an opening, but due to their increased strength and stiffness, exhibit a lower sensitivity to light damage when exposed to seismic ground motions as evaluated with calibrated finite element models.

Data availability statement

Some or all data, models, or code generated or used during the study are available from the corresponding author by request.

- Experimental values of force-drift,
- Experimental loading protocol,
- Experimental photographs used for DIC (pre-processed),
- Experimental displacement fields (post-processed by DIC),
- DIANA model files for main calibration models.

CRediT authorship contribution statement

Paul A. Korswagen: Conceptualization, Methodology, Software, Formal analysis, Investigation, Writing - original draft, Visualization. **Michele Longo:** Methodology, Software, Formal analysis, Investigation, Writing - original draft, Visualization. **Jan G. Rots:** Writing - review & editing, Supervision, Funding acquisition.

Acknowledgements

This research was funded by Nederlandse Aardolie Maatschappij (NAM) under contract number UI67339 'Damage sensitivity of Groningen masonry building structures – Experimental and computational studies', contract holders: Jan van Elk and Jeroen Uilenreef. This cooperation is gratefully acknowledged. The authors also express their gratitude to Edwin Meulman for his extensive support in designing, conducting and interpreting the laboratory experiments.

Appendix A. Supplementary material

Supplementary data to this article can be found online at https://doi.org/10.1016/j.engstruct.2020.110365.

References

[1] Anthoine A, Magonette G, Magenes G. Shear-compression testing and analysis of brick masonry walls. 10th European conference on earthquake engineering. Balkema, Rotterdam: Duma; 1995. ISBN 90 541o528 3.
[2] den Bezemer T, van Elk J. Special report on the Zeerijp Earthquake – 8th January 2018. NAM; 2018.
[3] Bindiganavile-Ramadas S. A hyperbolic model for degradation in tension mode-I fracture of masonry – implementation and validation in engineering masonry model. Delft University of Technology; 2018.
[4] Blaber J, Adair B, Antoniou A. Ncorr- open-source 2D digital image correlation Matlab software. Exp Mech 2015. https://doi.org/10.1007/s11340-015-0009-1.
[5] Boscardin MD, Cording EJ. Building response to excavation-induced settlement. J Geotech Eng 1989;115(1):1–21.
[6] Bosiljkov V, Page AW, Bokan-Bosiljkov V, Zarnić R. Evaluation of the seismic performance of brick masonry walls. Struct Control Health Monit 2010; 17:100–118 Published online 22 December 2008 in Wiley InterScience (www.interscience.wiley.com). DOI: 10.1002/stc.299.
[7] Cornelissen HAW, Hordijk DA, Reinhardt HW. Experimental determination of crack softening characteristic of normal weight and lightweight concrete. Heron 1986;31(2):45–56.
[8] Crammond G, Boyd SW, Dulieu-Barton JM. Speckle pattern quality assessment for digital image correlation. Opt Lasers Eng 2013;51(2013):1368–78.
[9] Crowley H, Polidoro B, Pinho R, van Elk J. Framework for developing fragility and consequence models for local personal risk. Earthquake Spectra 2017. https://doi.org/10.1193/083116EQS140M.
[10] Crowley H, Pinho R, Van Elk J, Uilenreef J. Probabilistic damage assessment of buildings due to induced seismicity. Bull Earthq Eng 2018. https://doi.org/10.1007/s10518-018-0462-1.
[11] Dhanasekar M, Prasad P, Dorji J, Zahra T. Serviceability assessment of masonry

arch bridges using digital image correlation. J. Bridge Eng 2019;24(2):04018120.
[12] Didier M, Abbiati G, Hefti F, Broccardo M, Stojadinovic B. Damage quantification in plastered unreinforced masonry walls using digital image correlation. 10th Australasian masonry conference, 14–18 February, 2018. 2018.
[13] Esposito R, Terwel K, Ravenshorst GJP, Schipper HR, Messali F, Rots JG. Cyclic pushover test on an unreinforced masonry structure reseambling a typical Dutch terraced house. 16th world conference on earthquake engineering, Santiago, Chile. 2017.
[14] Esposito R, Jafari S, Ravenshorst GJP, Schipper HR, Rots JG. Influence of the behaviour of calcium silicate brick and element masonry on the lateral capacity of structures. 10th Australasian masonry conference, Sydney, Australia. 2018.
[15] Giardina G, van de Graaf AV, Hendriks MAN, Rots JG, Marini A. Numerical analysis of a masonry façade subject to tunnelling-induced settlements. Eng Struct 2013;54(2013):234–47.
[16] Godio M, Vanin F, Zhang S, Beyer K. Quasi-static shear-compression tests on stone masonry walls with plaster: influence of load history and axial load ratio. Eng Struct 2019;192(2019):264–78.
[17] Graziotti F, Rossi A, Mandirola M, Penna A, Magenes G. Experimental characterisation of calcium-silicate brick masonry for seismic assessment. 16th International Brick and Block Masonry conference. 2016. ISBN 978-1-138-02999-6.
[18] Graziotti F, Tomassetti U, Kallioras S, Penna A, Magenes G. Shaking table test on a full scale URM cavity wall building. Bull Earthq Eng 2017;15(12):5329–64.
[19] Jafari S, Esposito R. Summary of material properties of existing Dutch masonry – updated URM abacus (version 2). Delft University of Technology; 2019. Report number C31B67WP1-16, version 02.
[20] Kallioras S, Guerrini G, Tomassetti U, Marchesi B, Penna A, Graziotti F, et al. Experimental seismic performance of a full-scale unreinforced clay-masonry building with flexible timber diaphragms. Eng Struct 2018;161(2018):231–49.
[21] Korswagen PA, Meulman E, Longo M, Rots JG. Crack initiation and propagation in unreinforced masonry structures subjected to repeated load and earthquake vibrations. 10th international masonry conference, Milan, Italy. 2018.
[22] Korswagen PA, Longo M, Meulman E, Rots JG. Crack initiation and propagation in unreinforced masonry specimens subjected to repeated in-plane loading during light damage. Bull Earthq Eng 2019. https://doi.org/10.1007/s10518-018-00553-5.
[23] Lagomarsino S, Penna A, Galasco A, Cattari S. TREMURI program: An equivalent frame model for the nonlinear seismic analysis of masonry buildings. Eng Struct 2013;56(2013):1787–99.
[24] Laurin F, Charrier JS, Lévêque D, Maire JF, Mavel A, Nuñez P. Determination of the properties of composite materials thanks to digital image correlation measurements. Procedia IUTAM 2012;4(2012):106–15.
[25] Lourenço PB, Rots JG. Multisurface interface model for analysis of masonry structures. J Eng Mech 1997;123(7):660–8.
[26] Lourenço PB, Rots JG, Blaauwendraad J. Two approaches for the analysis of masonry structures: micro and macro-modeling. HERON 1995;40(4). ISSN 0046-7316.
[27] Magenes G, Calvi GM. In-plane seismic response of brick masonry walls. Earthquake Eng Struct Dyn 1997;26:109101112.
[28] Messali F, Rots JG. In-plane drift capacity at near collapse of rocking unreinforced calcium silicate and clay masonry piers. Eng Struct 2018;164(2018):183–94.
[29] Messali F, Esposito R, Jafari S, Ravenshorst G, Korswagen PA, Rots JG. A multiscale experimental characterization of Dutch unreinforced masonry buildings. 16th European conference on earthquake engineering, Thessaloniki. 2018.
[30] Morandi P, Albanesi L, Graziotti F, Li Piani T, Penna A, Magenes G. Development of a dataset on the in-plane experimental response of URM piers with bricks and blocks. Constr Build Mater 2018;190(2018):593–611.
[31] Nepveu M, van Thienen-Visser K, Sijacic D. Statistics of seismic events at the Groningen field. Bull Earthquake Eng 2016;2016(14):3343–62. https://doi.org/10.1007/s10518-016-0007-4.
[32] Noorlandt R, Kruiver PP, de Kleine MPE, Karaoulis M, de Lange G, di Matteo A, et al. Characterisation of ground motion recording stations in the Groningen gas field. J Seismol 2018;2018(22):605–23. https://doi.org/10.1007/s10950-017-9725-6.
[33] Petry S, Beyer K. Limit states of modern unreinforced clay brick masonry walls subjected to in-plane loading. Bull Earthquake Eng 2015;2015(13):1073–95. https://doi.org/10.1007/s10518-014-9695-9.
[34] Petry S, Beyer K. Cyclic test data of six unreinforced masonry walls with different boundary conditions. Earthquake Spectra 2015;31(4):2459–84.
[35] Rots JG, De Borst R. Analysis of concrete fracture in “direct” tension. Int J Solids Struct 1989;25(12):1381–94.
[36] Rots JG, Messali F, Esposito R, Jafari S, Mariani V. Computational modelling of masonry with a view to groningen induced seismicity. Leuven: 10th SAHC structural analysis of Historical Construction; 2016.
[37] Rots JG, Van Der Pluijm R, Vermeltfoort AT. Structural masonry - an experimental/numerical basis for practical design rules. Balkema; 1997. ISBN 90 5410 680 8.
[38] Rots JG, Invernizzi S, Belletti B, Hendriks MAN. Circumventing bifurcations in structural softening. Computational modeling workshop on concrete, masonry and on fiber-reinforced composites. 2019.
[39] Saloustros S, Pelà L, Cervera M, Roca P. An enhanced finite element macro-model for the realistic simulation of localized cracks in masonry structures: A large-scale application. Int J Archit Heritage 2018;12(3):432–47. https://doi.org/10.1080/15583058.2017.1323245.
[40] Sarhosis V, Dais D, Smyrou E, Bal IE. Evaluation of modelling strategies for estimating cumulative damage on Groningen masonry buildings due to recursive induced earthquakes. Bull Earthq Eng 2019. https://doi.org/10.1007/s10518-018-00549-1.
[41] Schreppers GMA, Garofano A, Messali F, Rots JG. DIANA validation report for masonry modelling. DIANA FEA report 2016-DIANA-R1601 TU Delft structural mechanics report CM-2016-17; 2016. 143 pp.
[42] Slobbe AT, Hendriks MAN, Rots JG. Systematic assessment of directional mesh bias with periodic boundary conditions: applied to the crack band model. Eng Fract Mech 2013;109:186–208.
[43] Spetzler J, Dost B. Probabilistic seismic hazard analysis for induced earthquakes in Groningen – update. KNMI report – PSHA Groningen; 2017 update.
[44] Thamboo JA, Dhanasekar M, Yan C. Flexural and shear bond characteristics of thin layer polymer cement mortared concrete masonry. Constr Build Mater 2013;46(2013):104–13.
[45] Tomassetti U, Correia AA, Marques A, Graziotti F, Penna A, Magenes G. Dynamic collapse testing of a full-scale URM cavity-wall structure. Anidis 2017, Pistoia. 2017.
[46] van Elk JF, Bourne SJ, Oates SJ, Bommer JJ, Pinho R, Crowley H. A probabilistic model to evaluate options for mitigating induced seismic risk. Earthquake Spectra 2019. https://doi.org/10.1193/050918EQS118M.
[47] Van Staalduinen PC, Terwel K, Rots JG. Onderzoek naar de oorzaken van bouwkundige schade in Groningen Methodologie en case studies ter duiding van de oorzaken. Delft University of Technology. Report number CM-2018-01, 11 July 2018 – Downloadable from www.NationaalCoordinatorGroningen.nl.
[48] Zahra T, Dhanasekar M. Characterisation of cementitious polymer mortar – Auxetic foam composites. Constr Build Mater 2017;147(2017):143–59.